Article

Lineament Extraction from Digital Terrain Derivate Model: A Case Study in the Girón–Santa Isabel Basin, South Ecuador

Michelle Del Pilar Villalta Echeverria [1], Ana Gabriela Viña Ortega [1,2], Erwin Larreta [1,3], Paola Romero Crespo [1] and Maurizio Mulas [1,4,*]

1   Facultad de Ingeniería en Ciencias de la Tierra (FICT), ESPOL Polytechnic University, Guayaquil P.O. Box 09-01-5863, Ecuador
2   Telford Geotechnical, 101-1428 Lorne St, Kamloops, BC V2C 1X4, Canada
3   Instituto de Investigación Geológico Energético (IIGE), Quito 170518, Ecuador
4   Instituto Panamericano de Geografía e Historia (IPGH), Guayaquil P.O. Box 09-01-5863, Ecuador
*   Correspondence: mmulas@espol.edu.ec; Tel.: +59-3998250529

Abstract: Geological lineaments are linear or curvilinear surfaces that are considered a superficial expression of discontinuities on the earth's surface. The extraction of lineaments from remotely sensed satellite data is one of the most frequently used applications of remote sensing in geology. This study focuses on the semi-automatic extraction of lineaments in the Girón–Santa Isabel basin using a Topographic Position Index (TPI). The lineaments were extracted in the PCI Geomatics 2016 software and analyzed in the ArcGIS and Rockworks software. Statistical and density map analyses of the lineaments were performed; then, these results were interpreted to obtain the geological lineaments. Finally, a bibliographic verification was carried out, and structures such as faults and folds were defined. The total number of geological lineaments was 76, and 71 of them were defined as faults, the longest with a length of 33 km. It was determined that the preferential orientation of the lineaments is NE–SW, which is consistent with the axis of the Girón–Santa Isabel basin. This methodology can be useful to optimize time and reduce costs when gathering the structural information of the study area in the first stage of geological and mining prospecting or the educational field.

Keywords: TPI; geological lineaments; automatic extraction; faults; GIS; Santa Isabel Basin

1. Introduction

The morphology of the earth's surface is influenced by the joint actions of the internal (tectonism and volcanism) and external processes (denudation/erosion) of the planet [1,2]. Geographic features are related to these processes, in addition to lithologies, structures present, and the distribution of soil or other unconsolidated surface material [3]. In the early 20th century, the word "lineament" was applied to the characteristics of the earth's surface [4]. Later, this term was expanded, and new definitions of lineaments emerged [5,6]. Lineaments are defined by [7] as any mappable linear feature of the earth's surface, differentiated by distinct patterns of features that are aligned in coherent rectilinear or slightly curvilinear structures.

According to their genesis, three types of lineaments are found: (1) geological lineaments, (2) morphostructural lineaments, and (3) non-geological lineaments. Geological lineaments are mappable linear surfaces, generally considered a superficial expression of the discontinuities of geological structures, such as faults, fractures, joints, or lithological limits [8]. The morphostructural/topographic lineaments are caused by geomorphological processes; they correspond to the linear features of valleys, river drainage systems, and ridges [7]. Finally, linear non-geologic features are those created by human activity, such as roads, railways, crop field boundaries, or any changes in land use patterns [9].

Morphostructural lineaments can have a good equivalence with tectonic structures, such as fractures and faults [10,11]. These can be identified by the presence of rupture

figures and characteristic displacements on the surface and can be inferred by the presence of topographic and morphological features such as slope changes, fault scarps, depressions, and valleys [12]. Furthermore, these features include vegetation and soil moisture, which can be studied using the attributes of hue, color, texture, pattern, and topography [13,14].

Thus, by applying remote sensing and geomatic techniques in the structural analysis of the earth's surface, it is possible to map the characteristics of the terrain [15]. This facilitates obtaining structural and geological information from large or difficult-to-access areas through remotely sensed data, Geographic Information Systems (GIS), and database management [16]. In remote sensing, various methods can detect geological lineaments; these techniques can be differentiated into three groups [9]:

1. Manual lineament extraction is applied when the main objective is to delineate geological features [17]. It uses image-filtering techniques, band analysis, and transformation, among others. It is performed with visual interpretation and the manual digitization of the lineaments by human operators [18,19].

2. Semi-automated lineament extraction is performed by analyzing digital images through an initial automated process (the detection and extraction of the lineaments) and a second phase that corresponds to the interpretation and addition of the detected lineaments. This last step is performed by an operator [20,21] since after extracting the lineaments, manual editing is required to achieve a complete and correct set of linear features [22].

3. Automated lineament extraction is performed by analyzing digital images thanks to computer-assisted software. This automated processing includes the development of various algorithms responsible for improving the image, filtering, and detecting edges; it concludes with the extraction of lineaments and delivers the final lineament map in vector format. Some algorithms can be used, such as Hough Transform [23], Segment Tracing Algorithm (STA) [20], Lineament Extraction and Stripe Statistical Analysis (LESSA) [24], Canny Algorithm [25], and Lineament Detection and Analysis (LINDA) [26]. According to [27], the automated algorithms implemented in the extraction of lineaments consider the noise, the threshold, the size, and the orientation of the linear features. The automatic extraction process depends on the efficiency of these algorithms, as well as the content of the information present in the base image [28].

Automated extraction generates results in less time and detects more structures than manual detection. However, although automated lineament extraction methods help the analyst to produce the result in less time, they still have drawbacks since the extracted lines do not usually correspond to the geological structures of the analyzed area. Therefore, the user or analyst must evaluate the extracted lineaments or integrate the manual interpretations. For many years, researchers performed the visual interpretation and extraction of lineaments manually, as this was the conventional methodology; however, the influence and growth of technological progress have taken this process from the interpretation of aerial photographs using stereoscopes to the analysis and interpretation of remotely sensed data [29] (satellite images, digital elevation models (DEM), and digital terrain models (DTM) on computers) [30–36]. As a result, implementing semi-automatic and automatic methodologies is becoming more common due to timesaving and the optimization of results. These processes generally use satellite images (Landsat, ASTER, and Sentinel, among others), DEM, and Hillshade (shaded relief model) [3].

Nevertheless, the use of these inputs has important considerations. Interpretations of lineaments made on aerial photos and satellite images are biased due to the sun's position. These images provide a spectrum of information that includes anthropogenic features [9]. If hillshade is used, an analysis must be carried out, and a set of shaded relief models must be used since the information in these models depends on the direction of illumination. Therefore, the result obtained is influenced by the sun's azimuth, the slope, and the vertical exaggeration with which the hillshade is generated. That is, several models must be developed to ensure a better result.

An essential point when using DEMs (especially DEMs that result from RADAR data, for example, the DEM ALOS PALSAR) as inputs in the detection of lineaments is that the elevation data are based solely on natural topographic information. Then, data corresponding to manmade features such as streets, canals, field boundaries, etc., will not be presented when obtaining the lineaments. Furthermore, the resolution in the source data is a limitation in the structural interpretation of landforms [37]. This limitation is related to the remote sensing techniques used and the auxiliary information (maps, geological data, maps, and field observations) that can support the interpretation. Therefore, the present study proposes a semi-automated methodology to extract geological lineaments using remote sensing and GIS data.

Bearing in mind the considerations mentioned about satellite images and hillshade, in our study, we propose performing the analysis and automatic lineament extraction with a Topographic Position Index model (TPI) derived from a DEM. The important thing about using this model as a base image is that the TPI homogenizes the topography, discretizing the area and enhancing the relief so that mountaintops and valleys are more clearly differentiated, so only a TPI is generated from the DEM [38]. Therefore, this study aims to extract geological lineaments from the Santa Isabel–Girón Basin using remote sensing data and GIS technology, combined with statistical analysis and photogeological interpretation, to understand the spatial concentration and orientation of the lineaments in the study area.

2. Geomorphological and Geological Settings

The Girón–Santa Isabel area (Figure 1) is located in the southern inter-Andean region of Ecuador in the province of Azuay. It comprises 2304 km^2 of different landforms due to climatic, lithological, and tectonic factors.
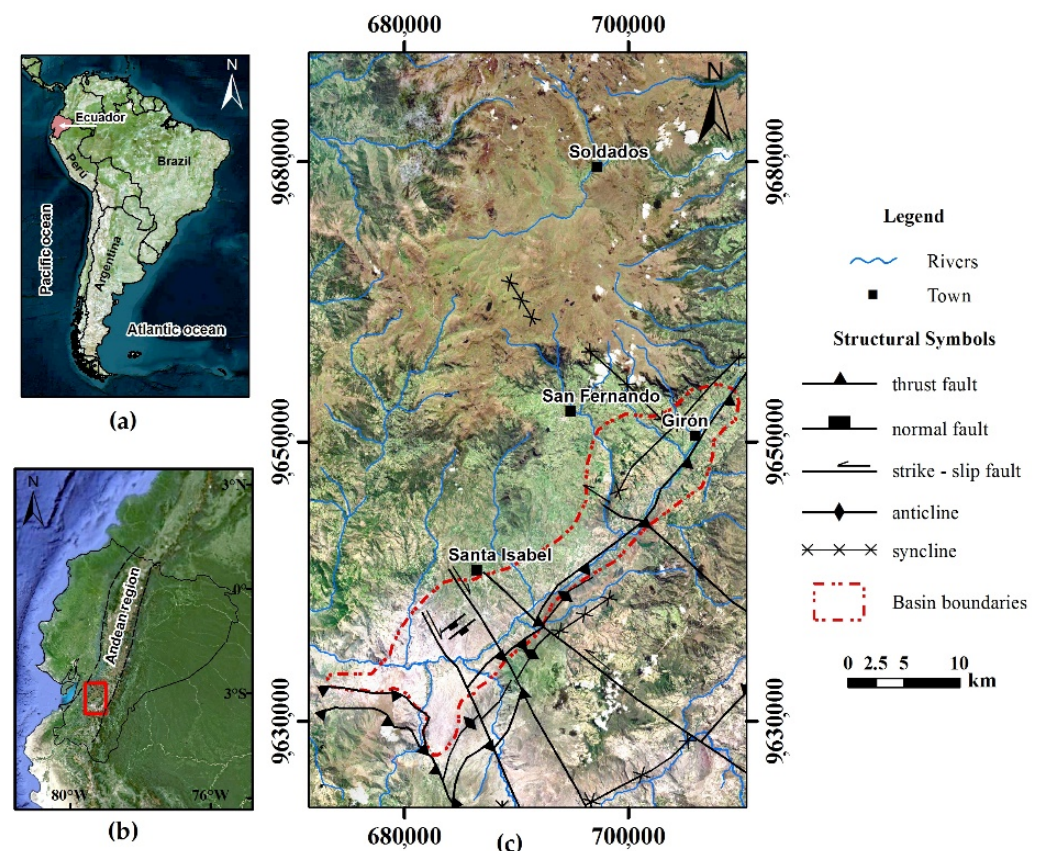

Figure 1. The studied area is located in Ecuador (**a**), in the area of Azuay (**b**) in the Santa Isabel–Giron basin (**c**).

2.1. Geomorphology

The relief is generally hilly and mountainous with an intermountain valley (the Girón–Santa Isabel Basin). The study area is between 833 to 4265 m above sea level. The higher areas rise steeply from the central zone to the northwest of the study site. The geomorphology of the sector is characterized by relatively steep slopes (slope 30–80°) in the northeast, southcentral, and southeast and an almost flat plateau with a gentle slope northcentral (Figure 2b) of the study area. In the northwest sector, there is a piedmont that corresponds to the foothills of the Western Cordillera toward the coastal plain. In the northcentral sector, the Quimsacocha Caldera is present. Due to the presence of this caldera, radial drainage can be observed in this sector. In addition, dendritic, rectangular, and parallel drainage systems are also present within the sector (Figure 2a). The Girón–Santa Isabel Basin drains toward the Pacific Ocean in the west via the Jubones River, which deeply incises the Cordillera Occidental.
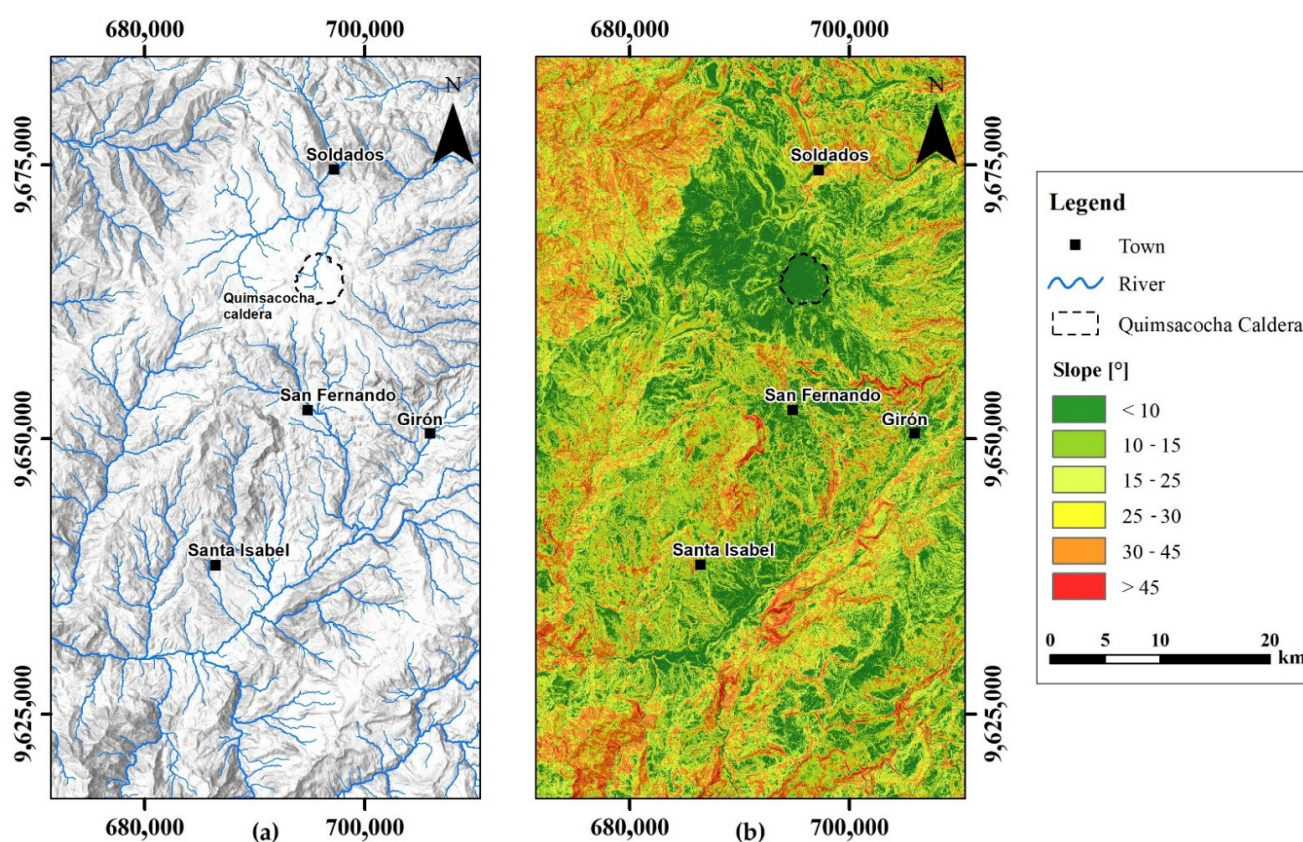

Figure 2. (**a**) Drainage system and (**b**) slope model of the study area.

2.2. Geological Setting

The Girón–Santa Isabel Basin is a Middle Miocene basin, and its fill overlies the Lower Oligocene volcanics with a distinct onlap. The basin accumulates coastal, alluvial, estuarine, lacustrine, and volcaniclastic sediments [39–41].

2.2.1. Middle Miocene Extension

The Girón–Santa Isabel Basin (Figure 3) is interpreted as a half-graben formed in the early Middle Miocene (around 15 Ma). The extensional setting was active until the early Late Miocene (10 Ma) [42], and it caused an intramountain basin formation. The Girón–Santa Isabel Basin is NE–SW directed. The normal faults, located near the town of Santa Isabel, have a NE–SW trend (parallel to the basin axis). On the normal faults, no strike-slip components are observed.
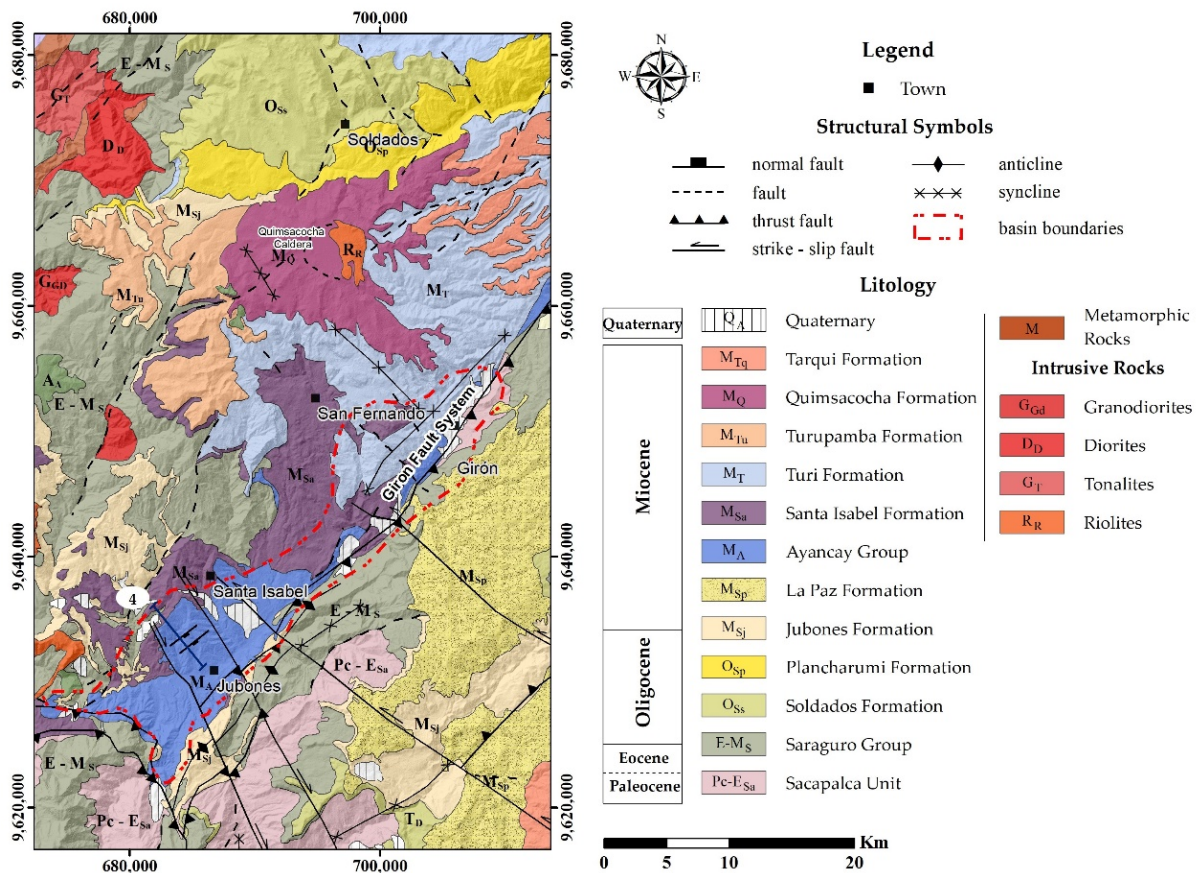
Figure 3. Geological map of the Girón–Santa Isabel Basin modified by [39,41].

In the southern part of the Girón–Santa Isabel Basin, the basin forms an extension and a subsequent deformation. In the "Quebrada Burrohuaycu", which lies south of the town of Santa Isabel (Figure 4) along the northwestern basin margin, the Middle Miocene basin fill overlies the Lower Oligocene volcanics with a distinct onlap. The Middle Miocene sediments wedge toward the southeastern basin margin and, therefore, the basin fill has a dominant asymmetric geometry. The asymmetric basin geometry implies a master normal fault at the southeastern margin. This fault is not exposed because of the younger compressional deformation, which resulted in a considerable shortening perpendicular to the basin axis. The basin is much larger than the present geographic area suggests, and the current limits are controlled by younger tectonic structures [41]. This is evidenced by the presence of relic sediments outside of the main depression.
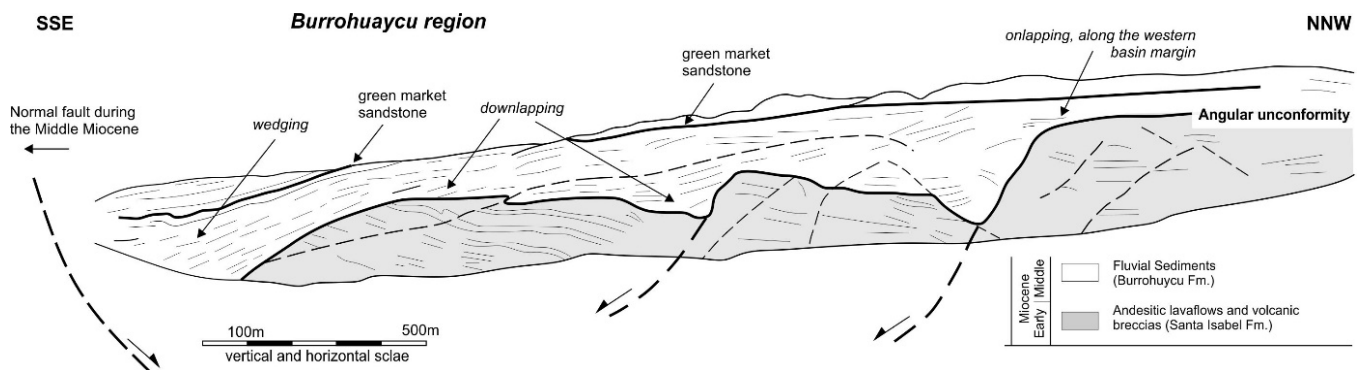

Figure 4. Cross-section of the Girón–Santa Isabel basin along the Quebrada Burrohuaycu, showing normal faulting. Modified by [41].

2.2.2. Late Miocene—Compression

A deformation event occurred around 9–8 Ma. The compressive deformation was characterized by large-scale (metric to regional scale) thrust faulting, reverse faults, and folding in the middle and lower Upper Miocene sediments and the underlying volcanic rocks. This compressional event caused the inversion of the Middle to early Late Miocene basins in the Andean domain and in the fore-arc region. Therefore, the extensional structures, which were formed during the Middle Miocene, were overprinted, and today, they are hard to reconstruct.

The youngest tectonic structures in the region are strike-slip faults with different trends and shear directions. In the area of Santa Isabel, the NW–SE striking faults are sinistral. A second group of NNW–SSE-trending faults possibly have a dextral displacement (Figure 2). These strike-slip faults cut the earlier Late Miocene compressional structures, and they are dated at 8 Ma [41].

3. Data and Methodology

The project methodology consisted of six parts: (i) data input and preparation; (ii) data preprocessing to obtain the base image; (iii) data processing for the automatic extraction of lineaments; (iv) postprocessing: statistical and photogeological analysis of the lineaments; (v) delimitation and verification; and (vi) the final product. Figure 5 illustrates the general flow diagram of the procedure executed in this study.
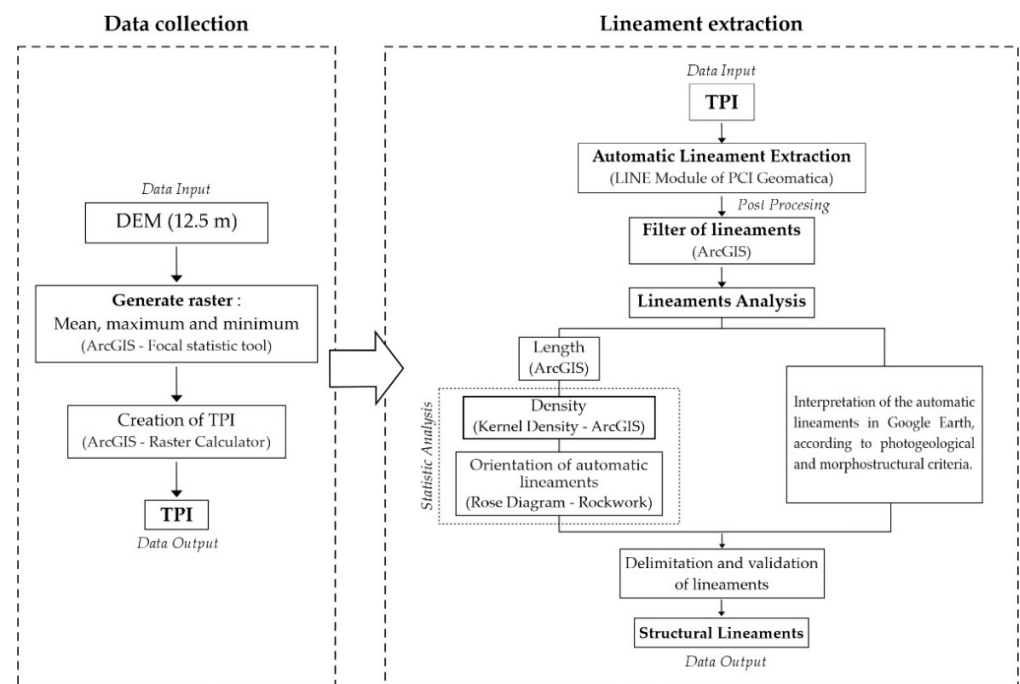

Figure 5. Methodology employed in this study.

3.1. Data Input

The geological data were obtained from the Geological Map of the Western Cordillera of Ecuador between −3 °, −4° S Scale 1: 200,000 by [39]. In addition, the structural map of the area was taken from [41]. The DEM base model used was the DEM ALOS (Advanced Land Observing Satellite) PALSAR (Phased Array Type L-Band Synthetic Aperture Radar), with 12.5 m spatial resolution obtained from NASA's Alaska Satellite Facilities open access platform. The DEMs ALPSRP248137120 and ALPSRP248137110 were acquired from the official website (https://search.asf.alaska.edu/#/ of NASA's Alaska Satellite Facility (ASF), accessed on 16 august 2021) [43].

The digital terrain model (Figure 6) was analyzed using the Topographic Position Index (TPI) (Figure 6c) with a raster cell size of 7 × 7. The TPI is defined as a dimensionless value

that groups the territory according to similar values. The TPI homogenizes the territory and generates a relief enhancement, which facilitates the recognition of morphostructural features. Results are obtained according to the cell size (pixel or distance) used in the neighborhood analysis performed by the TP. The larger the pixel size, the greater the generalization of the terrain and the lower the relief enhancement of the terrain. Wider ranges of values will generate a more general TPI, which does not enhance small geographic features [38]. The TPI model was obtained using the following equation:

$$TPI = \frac{DEM\,mean - DEM\,min}{DEM\,max - DEM\,min} \tag{1}$$

where DEM mean, DEM max, and DEM min represent the mean, maximum, and minimum values of the DEM. These rasters are generated with a chosen 7×7 matrix. This matrix has a pixel size equal to the original. Each of these raster images was obtained using the ArcGIS focal statistics tool.
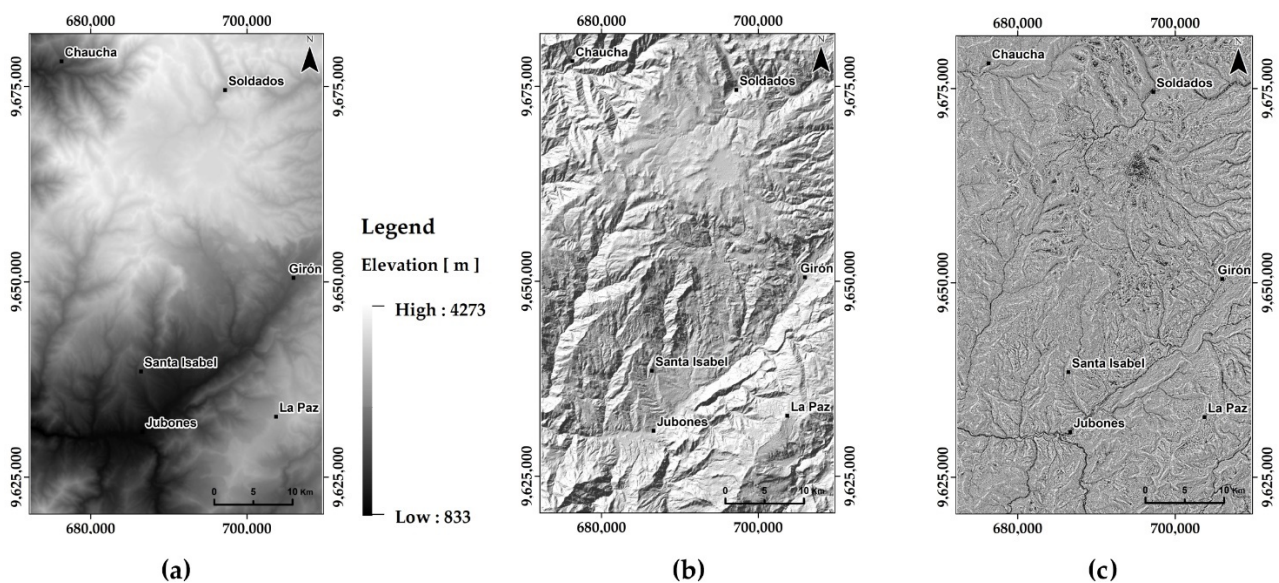

Figure 6. DEM and its derived models. (**a**) DEM ALOS PALSAR with a spatial resolution of 12.5 m; (**b**) hillshade model with an azimuth of 135°; and (**c**) TPI model.

3.2. Processing of Remote Sensing Data

Automatic lineament extraction was performed with the TPI model using the LINE module of the PCI Geomatics 2016 software (currently, the software is known as CATALYST Professional). This module is based on automatic detection algorithms. These algorithms are executed in three steps: edge detection, thresholding, and curve extraction. The LINE module extracts lineaments from an image and converts these linear features into vector form using six parameters [44–46]: RADI—radius of filter in pixels; GTHR—threshold for edge gradient in pixels; LTHR—threshold for curve length in pixels; FTHR—threshold for line-fitting error in pixels; ATHR—threshold for angular difference in degrees; and DTHR—threshold for linking distance in pixels.

The values assigned to each parameter are not fixed; they will vary according to the area and its topography, the resolution, and the type of image to be analyzed. By executing different sets of values in the six parameters, for our case study, the following was established (Table 1):

- The RADI represents the smallest level of detail that will be detected in the input image. That is, with this parameter, we establish the minimum length at which linearities will be detected. The value assigned to this parameter depends significantly on the image resolution and the working scale. For our case study, the TPI resolution is 12.5 m, and the working scale is (1:50,000); for this scale, anything smaller than 500 m

is not representative [47]. Therefore, 500 m will be considered the minimum detectable distance. This value in pixels corresponds to 40 pixels. Thus, the RADI parameter has a value of 40 pixels.

- GTHR and LTHR influence the number and length of the lines. The GTHR parameter is responsible for edge detection by thresholding the image [46]. This threshold value represents the minimum value (in terms of color) at which changes between two levels or a grayscale with high contrast will be recognized. This value should be in the range of 0 to 255 (Figure 5). The GTHR value is kept at 100, which is the value suggested by the program.

- The value assigned to the LTHR parameter represents the minimum length of the lines extracted by the LINE module. Since the scale of presentation is 1:100,000, anything less than 1000 m is not representative [47]. Therefore, this distance was used as the minimum length to be considered a lineament. Given our image resolution (12.5 m), 1000 m equals 80 pixels.

- FTHR influences accuracy. If high values are assigned to this parameter, longer lines are generated but with a poorer fit. A better fit is obtained with lower values, even though shorter line segments will be obtained. According to [48], values between 3–5 are considered adequate for remote sensing data.

- ATHR is the parameter that influences the joining of lineaments. It represents the maximum angle (in degrees) between segments or vectors to be joined. If the angle between two polyline segments does not exceed the given maximum value, the polyline is joined, resulting in longer lines. On the contrary, if they form an angle greater than the specified maximum, the polyline separates and generates shorter vectors. Hence, a value of 35° is used for this parameter.

- The DTHR parameter sets the separation between the lines. If two segments of a line are close to each other and the separation between them does not exceed the maximum indicated, the segments are linked and form a longer line. For our process, the value of 40 pixels was assigned since it represents the minimum length detected during the analysis.

- The resulting polylines are saved as a vector segment, and the software supports saving them in shapefile format.

Table 1. Parameters values of LINE Module.

Parameters	Default Values	Suggested Values
RADI	10	40
GTHR	100	* 100
LTHR	30	80
FTHR	3	3
ATHR	30	35
DTHR	20	40

* Default values.

The high density of automatically extracted lineaments occurs because the PCI line module recognizes features found in areas within major ridge structures (ridge margins) and valleys throughout the study area [49].

3.3. Postprocessing

3.3.1. Filter of Lineaments

The vector results obtained during the automatic extraction phase will have been previously analyzed in terms of length and orientation to filter them and define those representative lineaments. Figure 7a shows the automatically extracted lineaments.

Considering the spatial resolution of the base model (12.5 m), the minimum length that can be automatically extracted in this process is 375 m [50,51]. However, due to the scale of work, 500 m was considered the minimum detectable distance, which corresponds

to the minimum mappable unit [52]. Given the presentation scale of 1:100,000, during the automatic extraction, linear features longer than 1000 m were considered lineaments.
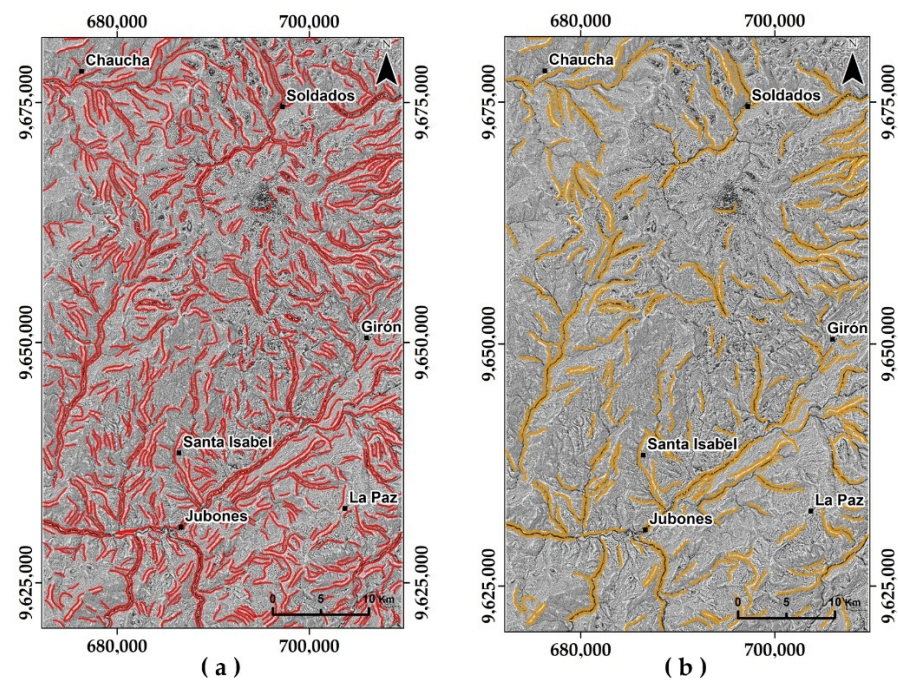

Figure 7. (**a**) Lineaments obtained with automated extraction. (**b**) Lineaments after filtering were considered lineaments of interest. Red lines are the automatic lineaments, and yellow lines are the lineaments of interest.

However, due to the extension of the study area (61.75 km × 37.30 km) and its morphology, 1000 m lines are not representative and constitute noise. Therefore, the Optimum Legible Delineation (OLD) was considered for the analysis of the lineaments. The OLD represents the optimal delineation size for a surface to be legible on a map; according to [53], the optimal length should be four times the minimum mappable unit. In our case, the OLD = 4 × 500 m = 2000 m.

Based on the above, in this study, we considered lineaments of interest, those with lengths greater than 2000 m (Figure 7b), to determine possible fault lines. For this purpose, lineaments with lengths less than 2000 meters were filtered. By filtering, we were able to better observe how the lineaments delimit the relief features in the TPI (Figure 7b). In addition, we noticed that the western and southern parts of the images exhibit longer lineaments than the northern and eastern parts.

3.3.2. Lineament Analysis

Quantitative and qualitative processes were carried out for the analysis of the lineaments. The first corresponds to a statistical analysis where the number, length, and density were analyzed based on calculations and processes carried out with ArcGIS software, version 10.8.2

- Line density analysis: Its purpose is to analyze the frequency of lines per unit area (number of lines/km^2) [54]. It is obtained by summing the length of available lineaments in a defined grid size (search radius). The lineament density is created with the Kernel density tool [55] of the spatial analyst tool in ArcGIS 10.8.2, with a search radius of 1.5 km according to [48].
- Lineament orientation: To know the direction of the lineaments in the study area, rose diagrams were generated [56] for the automatically generated lineaments and the lineaments of interest and, finally, to know the predominant orientation of the geological lineaments. These were elaborated in the Rockworks software, version 2016.

The qualitative analysis corresponds to the verification and interpretation of the lineaments of interest through satellite images and Google Earth. We analyzed how the lineaments relate to the morphostructural characteristics and the drainage network of the area. That is, we observed changes in the shape of the relief, very linear behavior, alignments of mountain tops, alignments of mountain ranges [57], terrain breaks, very deep and linear ravines (Figure 8a), abrupt changes in drainage patterns, and channel morphology (Figure 8b) [58,59].
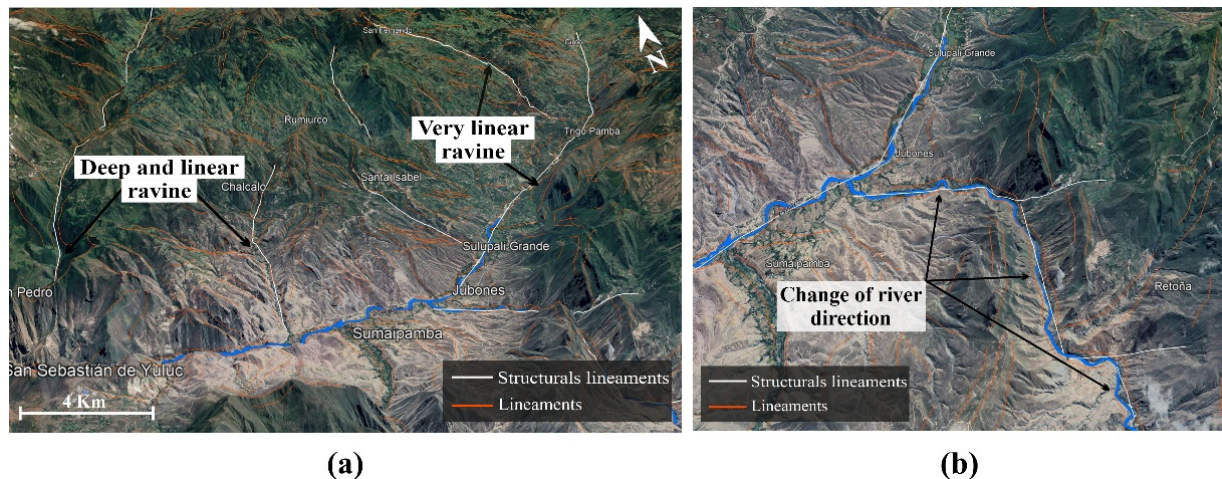

(a) **(b)**

Figure 8. Analysis of the study area using Google Earth. (**a**) Identification of streams with defined morphostructural features. (**b**) Recognition of changes in the direction of rivers.

3.4. Delimitation of Geological Lineaments

After obtaining the lineament density, the density map and the lineaments of interest were used as inputs to delimit the main geological lineaments in the study area. According to [33], lineament density provides valuable information on the intensity of tectonic deformation [33], fracture and rock shearing [55], and rock permeability [56]. Based on these, the first geological lineaments were drawn using the lineaments of interest as a guide that coincided with the zones of highest lineament density. Then, the previously obtained geological lineaments were analyzed in Google Earth and complemented with the qualitative analysis. After visualizing the lineaments of interest and the previously delimited geologic ones, new geologic lineaments were drawn based on the criteria explained in Section 3.3.2. The results of these analyses are presented in the following section.

3.5. Validation

The results of the geologic lineaments were validated by comparing them to the geologic mapping of the study area. They were compared with the geological maps of [39], the geological sheet of Cuenca (2017), and the structural map published by [41]. Finally, a fault diagram of the study area was made.

4. Results

4.1. Comparison

The lineaments extracted automatically from the TPI were compared with the lineaments obtained from other satellite images (Figure 7), in this case: DEM, a Landsat 8 image, hillshade of 45°, 315°, and multidirectional. The lineaments were extracted from these images using the same parameter values of the LINE module.

Of the automatic lineaments extracted from the five images, those obtained from the DEM (Figure 9c) have the shortest length and the greatest separation. From the hillshade results, we observed how the azimuth influences the orientation of the lineaments. For the 45° model, the detected lineaments present a predominant orientation in the NW–SE direction (Figure 9d), while the lineaments of the 315° hillshade present in the NE–SW

direction (Figure 9e). This means that the predominant orientation of the lineaments varies with the azimuthal angles. Therefore, when using the shaded relief model as a basis for lineament detection, at least eight azimuth directions must be analyzed for good and reliable results.
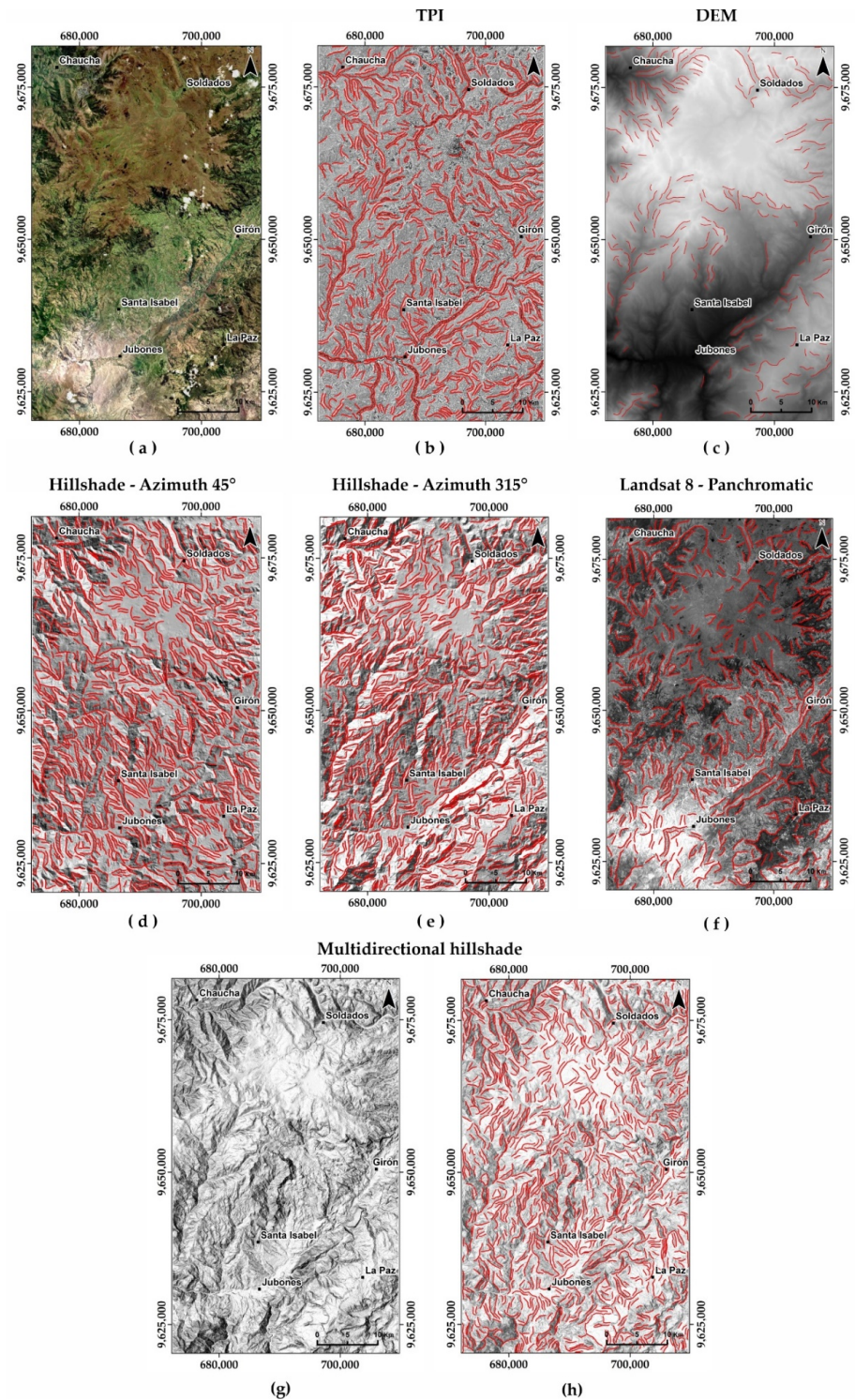
Figure 9. Comparison of the results of automatic extraction from different base images. Image (**a**) shows the study area, and (**g**) shows the multidirectional hillshade of the area. The others show the automatic lineaments obtained from (**b**) TPI, (**c**) DEM, (**d**) hillshade with an azimuth of 45°, (**e**) hillshade with an azimuth of 315°, (**f**) panchromatic from a Landsat 8, and (**h**) multidirectional hillshade. Red lines are the automatic lineaments.

It can also be observed that lineaments smaller than the average length (Table 2) represent 64% of the 45° hillshade and 66% of the total lineaments in the 315° hillshade. From the Landsat 8 image (Figure 9f), the lineaments were better adapted to the terrain characteristics, although these have little continuity; therefore, the length of these lines is shorter. The multidirectional hillshade in the Girón–Santa Isabel Basin zone reduces the slope change in the sectors near Jubones and Santa Isabel (Figure 9g). The areas with slopes comprise angles between 0–10°, and for slopes greater than 45°, valley areas lose details. This behavior is reflected in the median values of the lineament continuities (Figure 9h), obtained based on the multidirectional hillshade model (Table 2). An important consideration when using optical satellite imagery (e.g., Landsat or Sentinel) is to differentiate those lineaments that may result from human activity (roads, plantations, canals, etc.). Based on the automatic extraction of lineaments from the TPI (since this model homogenizes the territory and enhances the linear characteristics of the area), the lineaments present a better adaptation to the characteristics of the surface. This is not influenced by biases in altitude, illumination, or linearities resulting from human activity.

Table 2. Basic statistics of the automatically extracted lineaments from the remotely sensed image.

	TPI	DEM	Hillshade 45°	Hillshade 315°	Multidirectional Hillshade	Landsat 8—Panchromatic
No. of lineaments	1055	271	1261	1297	1213	653
Max. length (km)	14.23	6.53	8.35	11.78	9.99	10.23
Min. length (km)	1.00	1.00	1.00	1.00	1.00	1.20
Median length (km)	1.56	1.63	1.63	1.57	1.52	1.75
Mean length (km)	1.94	2.01	1.95	1.92	1.77	2.04

This comparison shows that, by using the TPI as the base image for the automatic detection of lineaments, the results and optimization of the process are simpler and faster to obtain.

It should be noted that, when using the PCI Geomatics LINE Module, the result obtained depends on the values assigned to the six parameters of this module. In turn, these parameters depend on the characteristics of the area, the objective of the study, and the resolution of the image used.

4.2. Postprocessing

The total number of lineaments obtained by the automated extraction process was 1055 (Figure 7a). Of these, 70.6% are shorter than 2000 m (Table 3). This first result shows that the maximum length of the linear structures was 14.23 km. As established in Section 3.3.1, the lineaments of interest for obtaining the geological lineaments were those longer than 2 km, representing 29.4% of the total (Table 3 and Figure 10).

Table 3. Lineament length class of automatically extracted lineaments.

Lineament Length Class	Range	Number of Lineaments	
		(In nos.)	(in %)
Very short	<1500 m	496	47.01
Short	1500–2000 m	249	23.60
Medium	2000–3000 m	185	17.54
Long	3000–4000 m	65	6.16
Very long	>4000 m	60	5.69
Total		1055	100.00

The authors selected the classes under consideration based on [60].

Once the length of the lineaments used as a guide was established, the results were filtered, and lineaments shorter than 2 km were removed (Figure 7b), obtaining 310 lineaments with a median length of 2817 m and a mean of 3257 m.
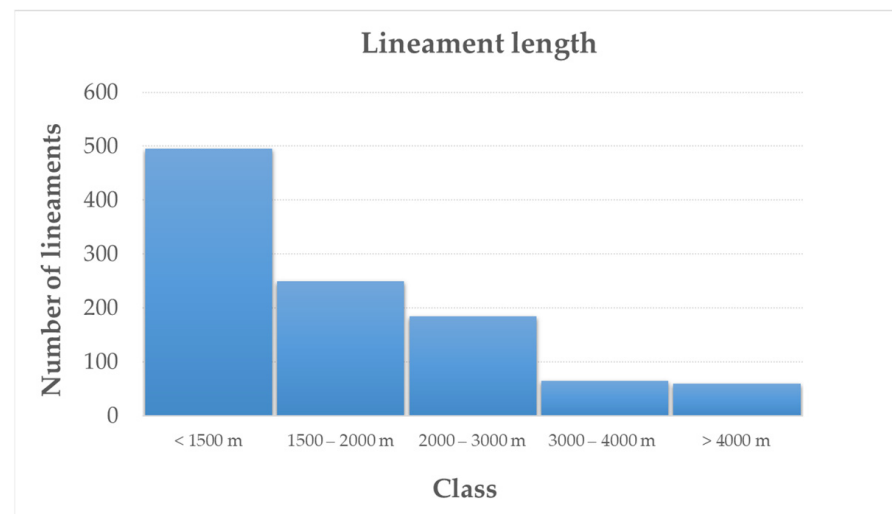
Figure 10. Lineament length histogram.

4.3. Lineament Density Map

After analyzing the basic statistics, the lineament density map was made with the lineaments of interest. Figure 11 shows the densest area, with a total length of more than 8 km to 17.7 km (dark blue color) in the northern and southcentral sectors of the study area. The density map was overlaid with lineaments, and their length in each grid was estimated (Figure 11a) to understand the spatial variation of lineament density in the study area. According to [60], the range of lineament density values obtained in the area of interest can be classified into five different categories: very low (<2 km/km^2), low (2 to 4 km/km^2), moderate (4 to 6 km/km^2), high (6 to 8 km/km^2), and very high (>8 km/km^2) lineament densities (Figure 11a). The very low-density category represents the largest area, covering 64.16% of the study area (Table 4). The low and moderate density categories cover 21.67% and 8.66% of the area. The categories that cover a relatively smaller area extension are the high and very high-density categories of lineaments, which cover 2.97% and 2.54%.
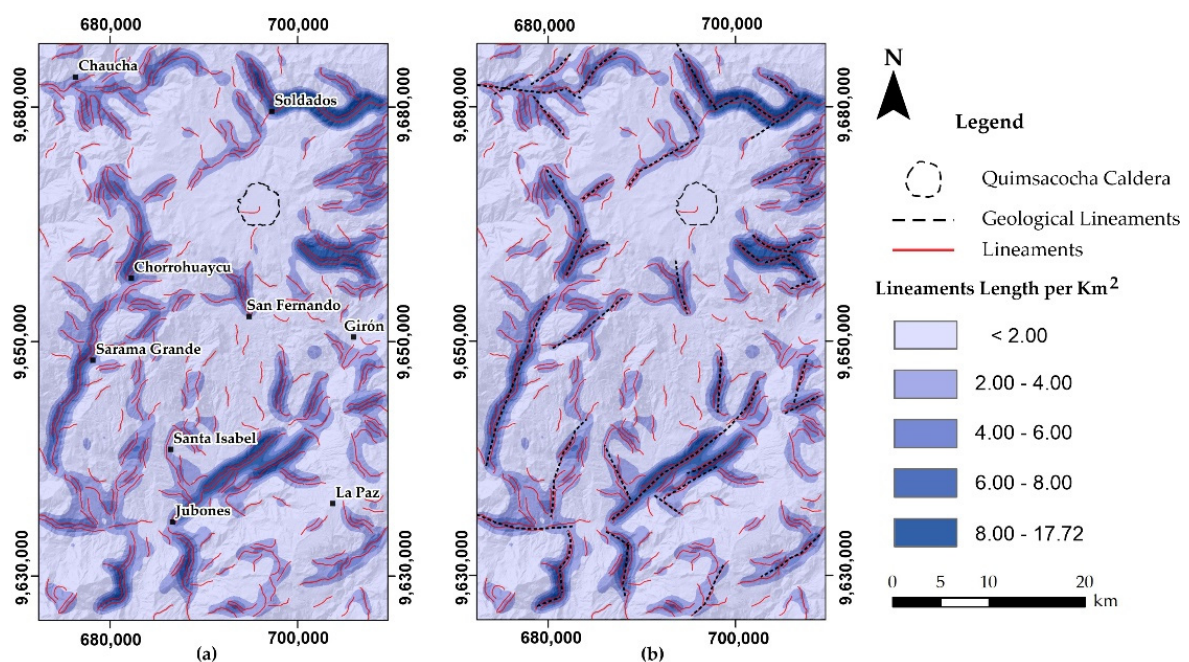

Figure 11. (**a**) Lineament density map of the automatically extracted lineaments. (**b**) The first delimitation of the geological lineaments.

Table 4. Area of lineament density classes.

Density Class	Density Range (km/km^2)	Area	
		(in km^2)	**(in %)**
Very low	<2	1479.65	64.16
Low	2–4	499.91	21.67
Moderate	4–6	199.74	8.66
High	6–8	68.45	2.97
Very high	>8	58.60	2.54
Total		2306.36	100.00

The authors selected the classes under consideration based on [60].

In the eastern flank zone of the Quimsacocha Caldera [39], a high-to-very-high density can be observed. The western sector of the study area presents zones in which the lineament density ranges from moderate to high. In the southeast and center of the area, a moderate-to-very-low density of lineaments can be observed. The sectors with the highest densities are: Soldados, Girón, Jubones, Chorrohuaycu, and Samara Grande (Figure 11a). The lineaments in areas of higher line density show a pattern that can be associated with fault zones. Therefore, these may be affected by greater structural deformation. According to our results, the zones of higher density coincide with the main faults and fault system of the area (the Girón Fault System) (Figure 3) [39,41]. Using the zones of high-density lineaments and the lineaments of interest as a guide, 47 lineaments were initially delimited, which will be referred to as geological lineaments (Figure 11b).

4.4. Orientation of the Lineaments

The automatically extracted lineaments were plotted using a rose diagram to understand their preferential orientations. The results were compared with the bibliographic information of the main orientation in the zone. The rose diagram was used for the total automatically extracted lineaments (Figure 12a) and those greater than 2000m (Figure 12b). The rose diagrams built for the different lineament length classes (Figure 12) show that, while very long lineaments are oriented predominantly in NE–SW directions, the shorter ones are oriented predominantly in NE–SW and NW–SE directions (Figure 12a). In both cases, it was observed that the predominant orientation of the automatic lineaments is NE–SW.
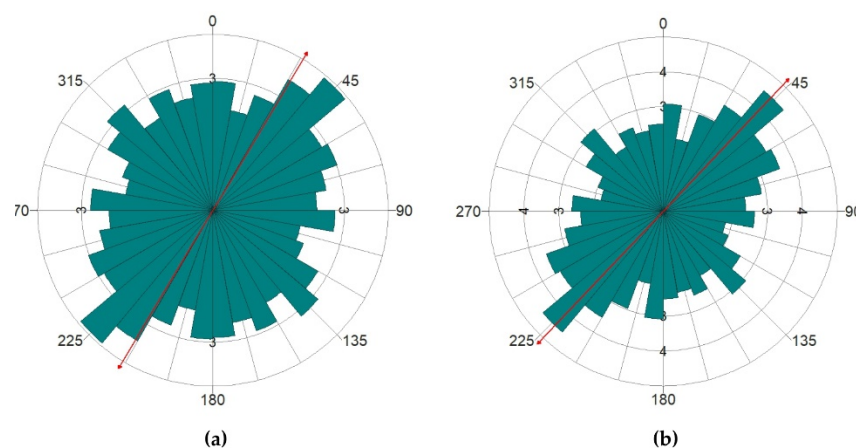

(a)　　　　　　　(b)

Figure 12. (**a**) Rose diagram showing the main trends obtained for the total automatic extraction lineaments; (**b**) rose diagram of automatically extracted lineaments greater than 2000 m.

4.5. Geological Lineaments

Based on the second part of the analysis and interpretation, 29 new lineaments were obtained, resulting in 76 geological lineaments in the study area. The new lineaments were obtained from the analysis of the density map. Qualitative analysis corresponds to the verification and interpretation of the lineaments of interest through satellite images and

Google Earth. After that, our result was compared with the geological and structural maps of the area [39,41] to correctly define the geological lineaments as tectonic structures (faults, fractures, anticlines, or synclines). The linearities obtained in this study are very similar to the reference data, and new geological lineaments were identified. However, it is also the case that, due to the limitations of being a purely digital analysis, there are features that are not possible to delimit and appear in the reference maps.

Finally, after the interpretation, comparison (Figure 11), and validation, 76 geological lineaments were recognized: 10 faults, 2 anticlines, 1 syncline, 61 inferred faults, and 2 leftover lineaments (Figure 13b). The results show that the maximum length of the linear structures (faults) is 33 km, and the average length is 6.8 km. In addition, they exhibit a preferential NE–SW orientation and an important family of NW–SE orientations (Figure 13c).
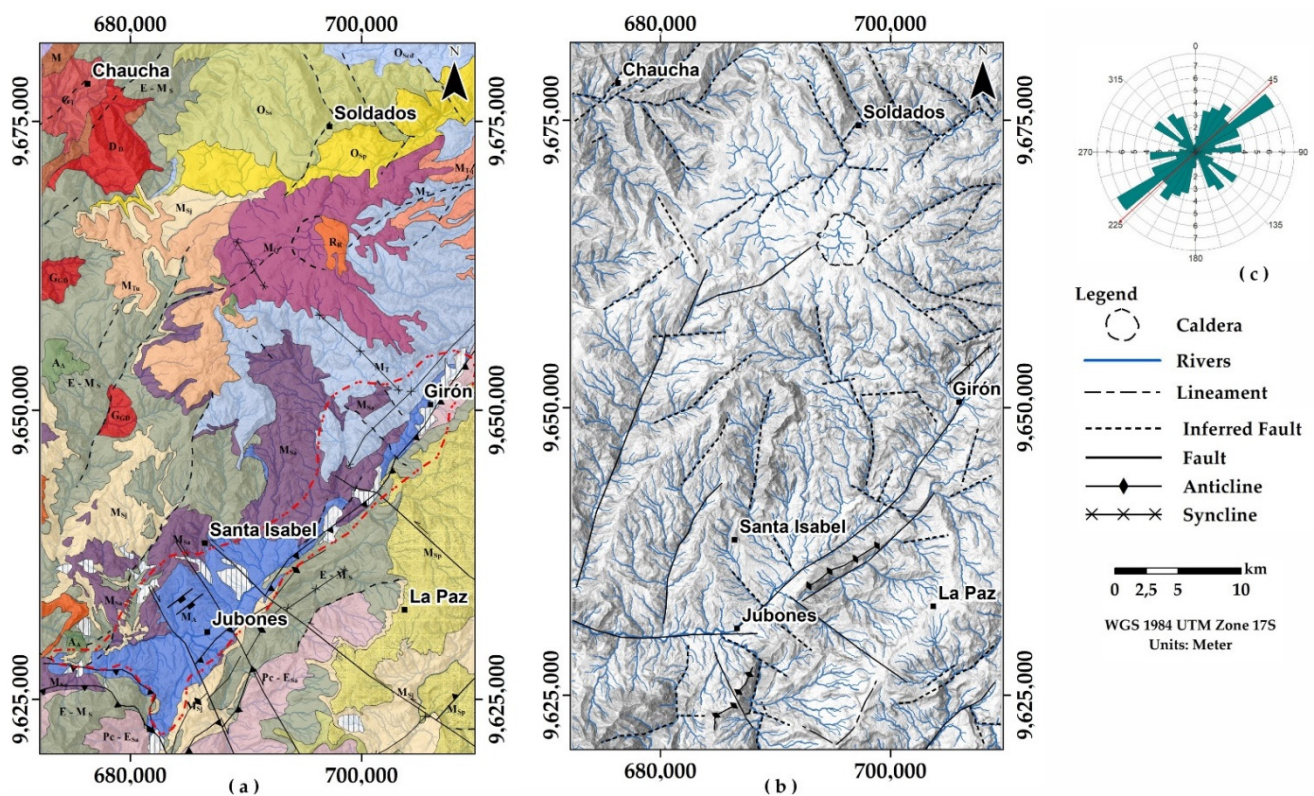

Figure 13. (**a**) Geological map of the area. (**b**) Structures obtained from the study area. (**c**) Rose diagram of inferred faults in the studied area. The legend of the geological map is shown in Figure 3.

5. Discussion

An automatic method of lineament extraction, presenting all possible linear features without discriminating manmade features, was successfully used in the mountainous area. The results showed an increase in the total number and length of lineaments.

By comparing the number, length, and predominant orientations of the lineaments extracted from the different remote sensing images, it was observed that lineament extraction should be performed considering different azimuthal angles or using an image that includes information on the linear features in different angles since, if an image with a preferential orientation is considered from the beginning, the result will be inadequate and overestimated. Therefore, TPI presents characteristics that facilitate the process of extracting linear features more accurately and reliably.

The analysis of automatic lineaments revealed that, in the study area, the short and very short lineaments represent a greater proportion, about 71% of the total lineaments; these being less than the Optimum Legible Delineation (OLD), they were not representative and, therefore, not used in the analyses. With the lineaments of interest, the zones with a high density of lineaments were analyzed since these may reflect zones with a high degree

of fracturing/rock-cutting and greater deformation intensity [56]. These areas of high lineament density may be vulnerable to slope failure or landslides. This result is consistent with the conditions in the study area, considering that different sectors of Jubones, Santa Isabel, Girón, Chaucha, and Soldados are affected annually by landslides, especially along the roads. Some roads have been built along fault axes in the study area, for example, the Girón–Santa Isabel–Jubones Road. The Ecuadorian Construction Standard (NEC-2014), in its NEC-SE-DS: Seismic Hazard chapter, places the Girón–Santa Isabel Road in seismic zone II, corresponding to a "high" seismic zone due to the presence of active faults.

The faults obtained (Figure 13b) with our methodology coincide with the main faults established in the available literature on the area [46,48]. In addition, new faults were identified, which were defined as inferred faults since they must be verified in the field. The structural data obtained from [48] and the geologic map of [46] (Figure 3) indicate that the preferential direction of the main regional structures of the Girón–Santa Isabel Basin is NE–SW, which is consistent with the results of the orientations in this study, with the Girón Fault System being the most representative.

6. Conclusions

The automated extraction of the linear features of an area will depend on the resolution and the satellite image used. DEM, DTM, and, in this case, TPI represent important tools for mapping morphostructural lineaments in difficult-to-access areas, tropical areas, and areas of high cloud cover, where the application of optical images can be difficult, as well as overcoming limited parameters established in the software used or the algorithm of the method employed. To obtain more reliable results, an operator must analyze and interpret the automated data obtained. In this way, the analysis of lineaments, as well as zones of high- and very-high-density lineaments, together with other morphostructural evidence, could be used as indicators of structural deformation in the study area.

In the methodology developed, 76 geological lineaments were obtained, and 71 faults (10 faults and 61 inferred faults) were defined from them. In general, they had an orientation and magnitude in accordance with the structures of the existing geological maps.

The present study provides a new database of lineaments for the Girón–Santa Isabel basin area that could be useful for developing management and development plans. The methodology developed in this study can be an efficient means to extract and analyze geological lineaments in large, difficult-to-access regions or those with few outcrops. This allows us to optimize time and reduce costs when collecting structural information on the study area in the first stage of geological, civil, and mining prospecting or the educational field. Furthermore, it offers a method that combines the automatic extraction of lineaments with the analysis of geospatial data (length, density, orientation, and trend) for the determination of fracture zones or faults.

Author Contributions: Conceptualization, M.D.P.V.E., A.G.V.O., E.L., P.R.C. and M.M.; methodology, M.D.P.V.E., A.G.V.O., E.L. and M.M.; software, M.D.P.V.E., A.G.V.O. and E.L.; validation, M.D.P.V.E., A.G.V.O. and E.L.; formal analysis, M.D.P.V.E. and E.L.; investigation, M.D.P.V.E., A.G.V.O., E.L. and M.M.; writing—original draft preparation, M.D.P.V.E. and M.M.; writing—review and editing, M.D.P.V.E., A.G.V.O., E.L., P.R.C. and M.M.; supervision, M.M., and PR.; All authors have read and agreed to the published version of the manuscript.

Conflicts of Interest: The authors declare no conflict of interest.

References

1. Hobbs, W.H. *Earth Features and Their Meaning; An Introduction to Geology for the Student and the General Reader*, 1st ed.; McMillan: New York, NY, USA, 1912; p. 506.
2. Jordan, G.; Meijninger, B.M.L.; Hinsbergen, D.J.J.; Meulenkamp, J.E.; Dijk, P.M. Extraction of morphotectonic features from DEMs: Development and applications for study areas in Hungary and NW Greece. *Int. J. Appl. Earth Obs. Geoinf.* **2005**, *7*, 163–182. [CrossRef]
3. Tiren, S. *Lineament Interpretation. Short Review and Methodology*; Progress Report; Swedish Nuclear Fuel and Waste Management Co (SKB), Swedish Hard Rock Laboratory: Stockholm, Sweden, 2010; p. 42.
4. Hobbs, W.H. Lineaments of the Atlantic Border region. *Bull. Geol. Soc. Am.* **1904**, *15*, 483–506. [CrossRef]
5. Hills, E.S. *Elements of Structural Geology*, 2nd ed.; John Wiley and Sons: New York, NY, USA, 1972; p. 502.
6. Ramsay, J.; Huber, M. *The Techniques of Modern Structural Geology: Folds and Fractures*; Academic Press Inc.: London, UK, 1987; pp. 309–700.
7. O'leary, D.W.; Friedman, J.D.; Pohn, H.A. Lineament, linear, lineation: Some proposed new standards for old terms: Discussion. *Bull. Geol. Soc. Am.* **1976**, *89*, 1463–1469. [CrossRef]
8. Minár, J.; Sládek, J. Morphological network as an indicator of a morphotectonic field in the central Western Carpathians (Slovakia). *Z. Geomorphol. Suppl. Issues* **2009**, *53*, 23–29. [CrossRef]
9. Ahmadi, H.; Pekkan, E. Fault-Based Geological Lineaments Extraction Using Remote Sensing and GIS—A Review. *Geosciences* **2021**, *11*, 183. [CrossRef]
10. Morelli, M.; Piana, F. Comparison between remote sensed lineaments and geological structures in intensively cultivated hills (Moanferrato and Langhe domains, NW Italy). *Int. J. Remote Sen.* **2006**, *27*, 1463–1475. [CrossRef]
11. Pal, S.K.; Majumdar, T.J.; Bhattacharya, A.K. Extraction of linear and anomalous features using ERS SAR data over Singhbhum Shear Zone, Jharkhand using fast Fourier transform. *Int. J. Remote Sens.* **2006**, *27*, 4513–4528. [CrossRef]
12. Marchionni, D.S.; Cavayas, F. La teledetección por radar como fuente de información litológica y estructural: Análisis espacial de imágenes SAR de RADARSAT-1. *Geoacta* **2014**, *39*, 62–89.
13. Khan, S.D.; Glenn, N. New strike-slip faults and litho units mapped in Chitral (N. Pakistan) using field and ASTER data yield regionally significant results. *Int. J. Remote Sens.* **2006**, *27*, 4495–4512. [CrossRef]
14. Enoh, M.; Okeke, F.; Okeke, U. Automatic lineaments mapping and extraction in relationship to natural hydrocarbon seepage in Ugwueme, South-Eastern Nigeria. *Geod. Cartogr.* **2021**, *47*, 34–44. [CrossRef]
15. Lu, P.F.; An, P. A metric for spatial data layers in favorability mapping for geological events. *IEEE Trans. Geosci. Remote Sens.* **1999**, *37*, 1194–1198. [CrossRef]
16. Guoan, T. Progress of DEM and digital terrain analysis in China. *Acta Geogr. Sin.* **2014**, *69*, 1305–1325.
17. Das, S.; Pardeshi, S.D.; Kulkarni, P.P.; Doke, A. Extraction of lineaments from different azimuth angles using geospatial techniques: A case study of Pravara basin, Maharashtra, India. *Arab. J. Geosci.* **2018**, *11*, 160. [CrossRef]
18. Scheiber, T.; Fredin, O.; Viola, G.; Jarna, A.; Gasser, D.; Łapińska-Viola, R. Manual extraction of bedrock lineaments from high-resolution LiDAR data: Methodological bias and human perception. *GFF* **2015**, *137*, 362–372. [CrossRef]
19. Azman, A.I.; Talib, J.A.; Sokiman, M.S. The integration of remote sensing data for lineament mapping in the semanggol formation, Northwest Peninsular Malaysia. In *IOP Conference Series: Earth and Environmental Science*; Institute of Physics Publishing: Kuala Lumpur, Malaysia, 2020; Volume 540.
20. Koike, K.; Nagano, S.; Ohmi, M. Lineament analysis of satellite images using a Segment Tracing Algorithm (STA). *Comput. Geosci.* **1995**, *21*, 1091–1104. [CrossRef]
21. Suzen, M.L.; Toprak, V. Filtering of satellite images in geological lineament analyses: An application to a fault zone in Central Turkey. *Int. J. Remote Sens.* **1998**, *19*, 1101–1114. [CrossRef]
22. Bonetto, S.; Facello, A.; Ferrero, A.M.; Umili, G. A tool for semi-automatic linear feature detection based on DTM. *Comput. Geosci.* **2015**, *75*, 1–12. [CrossRef]
23. Wang, J.; Howarth, P.J. Use of the Hough Transform in Automated Lineament Detection. *IEEE Trans. Geosci. Remote Sens.* **1990**, *28*, 561–567. [CrossRef]
24. Soto-Pinto, C.; Arellano-Baeza, A.; Sánchez, G. A new code for automatic detection and analysis of the lineament patterns for geophysical and geological purposes (ADALGEO). *Comput. Geosci.* **2013**, *57*, 93–103. [CrossRef]
25. Marghany, M.; Hashim, M. Lineament mapping using multispectral remote sensing satellite data. *Int. J. Phys. Sci.* **2010**, *5*, 1501–1507. [CrossRef]
26. Masoud, A.; Koike, K. Applicability of computer-aided comprehensive tool (LINDA: Lineament Detection and Analysis) and shaded digital elevation model for characterizing and interpreting morphotectonic features from lineaments. *Comput. Geosci.* **2017**, *106*, 89–100. [CrossRef]
27. Joshi, A.K. Automatic detection of lineaments from Landsat data. *Dig. Int. Geosci. Remote Sens. Symp.* **1989**, *1*, 85–88.
28. Al-Dossary, S.; Marfurt, K.J. Lineament-preserving filtering. *Geophysics* **2007**, *72*, P1–P8. [CrossRef]
29. Abdullah, A.; Nasser, S.; Ghaleeb, A. Landsat ETM-7 for Lineament Mapping using Automatic Extraction Technique in the SW part of Taiz area, Yemen. *Glob. J. Hum. Soc. Sci. Res.* **2013**, *13*, 35–37.
30. Podwysocki, M.; Moik, J.; Shoup, W. Quantification of geological lineaments by manual and machine processing technique. In *NASA Earth Resources Survey Symposium*; NASA: Houston, TX, USA, 1975; pp. 885–903.

31. Parsons, A.J.; Yearley, R.J. An analysis of geologic lineaments seen on LANDSAT MSS imagery. *Int. J. Remote Sens.* **1986**, *7*, 1773–1782. [CrossRef]
32. Divi, R.S.; Zakir, F.A. Delineation of Tectonic Features Utilizing Satellite Remote Sensing Data: I-The Southern-Half of the Arabian Shield. *Gondwana Res.* **2001**, *4*, 159–161. [CrossRef]
33. Das, D.P.; Chakraborty, D.K.; Sarkar, K. Significance of the regional lineament tectonics in the evolution of the Pranhita-Godavari sedimentary basin interpreted from the satellite data. *J. Asian Earth Sci.* **2003**, *21*, 553–556. [CrossRef]
34. Pour, A.B.; Hashim, M. Structural mapping using PALSAR data in the Central Gold Belt, Peninsular Malaysia. *Ore Geol. Rev.* **2015**, *64*, 13–22. [CrossRef]
35. Scheiber, T.; Viola, G. Complex bedrock fracture patterns: A multipronged approach to resolve their evolution in space and time. *Tectonics* **2018**, *37*, 1030–1062. [CrossRef]
36. Abdelkareem, M.; Hamimi, Z.; El-Bialy, M.Z.; Khamis, H.; Abdel Wahed, S.A. Integration of remote-sensing data for mapping lithological and structural features in the Esh El-Mallaha area, west Gulf of Suez, Egypt. *Arab. J. Geosci.* **2021**, *14*, 497. [CrossRef]
37. Prasad, A.D.; Jain, K.; Gairola, A. Mapping of lineaments and knowledge base preparation using geomatics techniques for part of the Godavari and Tapi basins, India: A case study. *Int. J. Comput. Appl.* **2013**, *70*, 9.
38. Weiss, A. Topographic position, and landforms analysis. In Proceedings of the Poster Presentation, ESRI User Conference, San Diego, CA, USA, 9–13 July 2001; p. 200.
39. Pratt, E.; Figueroa, J.; Flores, B. Informe N° 1, proyecto de desarrollo minero y control ambiental, programa de información cartográfica y geológica: Mapa escala 1: 200.000. In *Geology of the Cordillera Occidental of Ecuador between 3° S and 4° S*; CODIGEM -BGS: Quito, Ecuador, 1997; p. 58.
40. Flor, A.; Avilés, H.; Villalta, M.; Murillo, I.; Larreta, E.; Mulas, M. Geotechnical and structural characterization of the Ignimbritas of the Saraguro group in the sector of Santa Isabel-Pucará, Ecuador. In Proceedings of the 17th LACCEI International Multi-Conference for Engineering, Education, and Technology, Montego Bay, Jamaica, 24–26 June 2019.
41. Hungerbühler, D. Neogene Basins in the Andes of Southern Ecuador: Evolution, Deformation, and Regional Tectonic Implications. Ph.D. Thesis, ETH Zurich, Zurich, Switzerland, 1997.
42. Siravo, G.; Speranza, F.; Mulas, M.; Costanzo-Alvarez, V. Significance of northern Andes terrane extrusion and genesis of the interandean valley: Paleomagnetic evidence from the "Ecuadorian orocline". *Tectonics* **2021**, *40*, e2020TC006684. [CrossRef]
43. PALSAR_Radiometric_Terrain_Corrected_high_res; Includes Material © JAXA/METI 2007. Accessed through ASF DAAC 04 Julio 2020. Available online: https://doi.org/10.5067/Z97HFCNKR6VA (accessed on 16 August 2021).
44. PCI Geomatics. *Geomatica Exploration and Geological Applications*; PCI Geomatics: Markham, ON, Canada, 2018.
45. PCI Geomatics. *Geomatica Training Guide*; Geomatica, I Course Guide; PCI Geomatics: Markham, ON, Canada, 2018.
46. PCI Geomatics. CATALYST: LINE. Available online: https://catalyst.earth/catalyst-system-files/help/references/pciFunction_r/easi/E_line.html (accessed on 12 February 2022).
47. Chuvieco, E. *Fundamentos de Teledetección Espacial*, 1st ed.; RIALP, S.A.: Madrid, Spain, 1996.
48. Hashim, M.; Ahmad, S.; Johari, M.A.M.; Pour, A.B. Automatic lineament extraction in a heavily vegetated region using Landsat Enhanced Thematic Mapper (ETM+) imagery. *Adv. Space Res.* **2013**, *51*, 874–890. [CrossRef]
49. El-Sawy, K.; Ibrahim, A.M.; El-Bastawesy, M.A.; El-Saud, W.A. Automated, manual lineaments extraction and geospatial analysis for Cairo-Suez district (Northeastern Cairo-Egypt), using remote sensing and GIS. *Int. J. Innov. Sci. Eng. Technol.* **2016**, *3*, 491–500.
50. Abdullah, A.; Akhir, J.M.; Abdullah, I. The Extraction of Lineaments Using Slope Image Derived from Digital Elevation Model: Case Study: Sungai Lembing—Maran Area, Malaysia. *J. Appl. Sci. Res.* **2010**, *6*, 1745–1751.
51. Abdullah, A.; Akhir, J.M.; Abdullah, I. Automatic Mapping of Lineaments Using Shaded Relief Images Derived from Digital Elevation Model (DEMs) in the Maran-Sungai Lembing Area, Malaysia. *Electron. J. Geotech. Eng.* **2010**, *15*, 949–957.
52. Salichtchev, K.A. *Cartografía*; Editorial Pueblo y Educación: La Habana, Cuba, 1979; p. 182.
53. Vink, A.P.A. *Land Use in Advancing Agriculture*; Springer: Berlin, Germany; New York, NY, USA, 1975; p. 394.
54. Greenbaum, D. Revisión de aplicaciones de sensores remotos para la exploración de aguas subterráneas en sótanos y regolito. *Br. Geol. Surv. Rep. OD* **1985**, *85*, 36.
55. Terrell, R.G.; Scott, D.W. Variable kernel density estimation. *Ann. Stat.* **1992**, *20*, 1236–1265. [CrossRef]
56. Chandrasekhar, P.; Martha, T.R.; Venkateswarlu, N.; Subramanian, S.K.; Kamaraju, M. Regional geological studies over parts of Deccan Syneclise using remote sensing and geophysical data for understanding hydrocarbon prospects. *Curr. Sci.* **2011**, *100*, 95–99.
57. Masoud, A.A.; Koike, K. Autodetection, and integration of tectonically significant lineaments from SRTM DEM and remotely sensed geophysical data. *ISPRS J. Photogram. Remote Sens.* **2011**, *66*, 818–832. [CrossRef]
58. Mandeng, E.; Bidjeck, L.; Wambo, J.; Tak, A.; Betsi, T.B.; Ipan, A.S.; Dieudonné, L. Lithologic and structural mapping of the Abiete–Toko gold district in southern Cameroon, using Landsat 7 ETM+/SRTM. *Comptes Rendus Geosci.* **2018**, *350*, 130–140. [CrossRef]
59. García, A.; Zamorano, J.J.; López-Miguel, C.; Galván-García, A.; Carlos-Valerio, V.; Ortega, R.; Macías, J.L. El arreglo morfoestructural de la Sierra de Las Cruces, México central. *Rev. Mex. Cienc. Geológicas* **2008**, *25*, 158–178.
60. Raj, N.; Prabhakaran, A.; Muthukrishnan, A. Extraction and analysis of geological lineaments of Kolli hills, Tamil Nadu: A study using remote sensing and GIS. *Arab. J. Geosci.* **2017**, *10*, 195. [CrossRef]